

Physics-Informed Domain Adaptation for Electrical Energy Monitoring

Aaron W. Langham, Thomas C. Krause, and Steven B. Leeb

Abstract—**C**hanging grid conditions challenge modeling assumptions for power systems. For example, electrical signatures may differ between “islanded” and “grid-connected” modes of a microgrid’s operation. Unmodeled variance and shifts in data distributions confound data-driven techniques that model practical physical systems. With proper preprocessing, knowledge of the system’s underlying physics can guide the training and use of data-driven models of load behavior to provide domain adaptation that “undoes” these effects. These adaptation techniques provide greater feature space separability, enabling better visualization, clustering, and load identification. This work presents a general technique for deploying physics-informed domain adaptation on monitoring systems for microgrids with evolving voltage conditions. Case studies across multiple types of electrical loads demonstrate that these techniques can remove significant standard deviation in electrical features, ranging here from a 37.8% to 89% reduction.

Index Terms—Power system measurements, nonintrusive load monitoring, domain adaptation

I. INTRODUCTION

Energy facilities of all kinds benefit from electrical monitoring. System faults that may not be obvious to watchstanders are often plainly visible in electrical data [1]–[3]. In particular, nonintrusive power monitoring provides a low-cost, scalable, and retrofittable solution capable of fault detection and diagnostics (FDD).

For example, gradual equipment degradation creates subtle changes in electrical signatures. A nonintrusive load monitor (NILM) can track these changes over time and provide automated condition monitoring. However, changes in an electrical system’s behavior due to reasons unrelated to load condition complicates monitoring. Benign deviations in electrical signature, such as varying load tasks or grid conditions, may obscure deviations in electrical signature due to faults.

Data-driven and machine learning techniques can help characterize the typical electrical behavior for a specific piece of equipment and the larger grid structure. However, statistical learning techniques are not always robust in handling future variability, whether pathological or healthy. In addition, modern deep learning methods are often designed to prioritize predictive performance rather than interpretability.

Data transformation and preprocessing are critical steps in automated and manual fault detection and data analysis on energy systems [4]. This is especially true on “nonstationary” systems, in which important physical and environmental system parameters fluctuate or drift over time. Preprocessing

techniques informed by nonintrusive system measurements can compensate for these nonstationary characteristics [5]. As an example, consider the supply voltage waveform on an arbitrary ac power system. The frequency of this waveform may remain in a tight tolerance, but the rms value will deviate from its nominal value by a considerable amount. To illustrate, IEEE standard 1547-2018 defines continuous operation mode for distributed energy resources as between 88% and 110% of the nominal voltage [6]. Although loads are typically designed to handle a range of rms voltages, their power signatures inevitably take different forms when the rms voltage changes. This lack of consistency creates problems for nonintrusive pattern recognition techniques [7], [8]. Signature variability due to grid conditions makes it difficult to characterize normal versus faulty electrical signatures. This paper presents contributions to NILM power data preprocessing to reduce the impact of grid variability on data classification, clustering, and visualization. The organization of the paper is as follows. Section II gives a literature review and background context for nonintrusive load monitoring and the contribution this work makes. Section III presents a functional technique for removing variance unrelated to load condition, including a parameter-free method. Section IV demonstrates a model-based compression technique and a case study on field data from a shipboard microgrid. Section V introduces a data-driven compression technique and a case study with a power electronic load. Section VI describes implementation details for these techniques.

II. BACKGROUND AND REVIEW

Power monitoring aims to infer grid and load conditions from a set of installed sensors. At the bulk power grid scale, this takes the form of phasor measurement units (PMUs), advanced metering infrastructure (AMI), and synchro-waveforms. PMUs provide utilities with information on power flow direction on and voltage angles [9]. AMI often takes the guise of “smart meters” installed on residential homes, providing utilities a coarse view into individual home power consumption profiles [10]. Synchro-waveforms provide time-aligned measurements of the actual grid waveforms at multiple locations [11]. At the other end of the spectrum, “intrusive load monitoring” measures individual load currents, allowing precise state tracking and condition monitoring for a set of loads [12]. However, the hardware requirements of this method scale unfavorably with the number of loads monitored.

A. W. Langham, T. C. Krause, and S. B. Leeb are with the Massachusetts Institute of Technology, Cambridge, MA 02139 USA (email: alangham@mit.edu)

A. Nonintrusive Monitoring

Nonintrusive load monitoring lies between these two approaches in sensor complexity. Individual load information is inferred from aggregate voltage and current sensing. First proposed by Hart [7], nonintrusive load monitoring has since been widely researched [13] and commercialized [14] for residential systems. Sequential deep learning techniques have become common in residential load disaggregation research [15]. Residential NILM techniques are typically trained and evaluated via supervised learning on publicly available benchmark datasets [8], [16]. In addition, most research focuses on the “load identification” or “energy disaggregation” problem, which seeks to itemize energy usage to each load on the system.

In contrast, industrial NILM research and applications have typically been more bespoke in their design. Common residential loads such as refrigerators, ovens, and air conditioners may be similar to how they appear in training datasets. However, industrial loads will frequently present an “evolving” profile over time as the load condition changes [17], [18]. Individual load signatures are typically not available before installing a NILM, so training a NILM must be done with a relatively scarce amount of data. Deep learning techniques have been proposed and evaluated in laboratory scenarios. However, practical applications are hindered by the low availability of representative training data. As a result, techniques such as correlation matching are typically used in NILMs deployed in the field [19]. In addition, much of the value provided by a NILM in an industrial site comes not only from load identification and energy disaggregation, but also from fault detection and diagnostics. Many studies have used electrical monitoring to detect pathologies such as bearing faults [20]. Nonintrusive fault detection and condition tracking can be performed, for example, by enumerating possible transient signatures for known load failure modes [21] or tracking load signature drift over time [17]. All of these tasks are frustrated by grid conditions that change over time.

B. Domain Adaptation

In machine learning, domain adaptation refers to the ability of a model to successfully perform a task on a distribution of data potentially different than the training data [22]–[24]. As an illustration, Fig. 1 shows an example of a “domain shift.” The initial training data, shown by the filled shapes, occupies a different region in some feature space than the test data, shown by the non-filled shapes. For this classification task, the decision boundary that separates the filled shapes performs poorly on the non-filled shapes. However, the right plot shows the data after being transformed into a new feature space. Here, the distributions of the circles and triangles are the same, and the decision boundary from training generalizes well to the test data.

Domain adaptation research in nonintrusive load monitoring typically seeks to preserve model performance when deployed on a dataset different than the training set [25]. For example, this may take the form of training a model on one building and testing it on a different building [26]. In [27], the authors

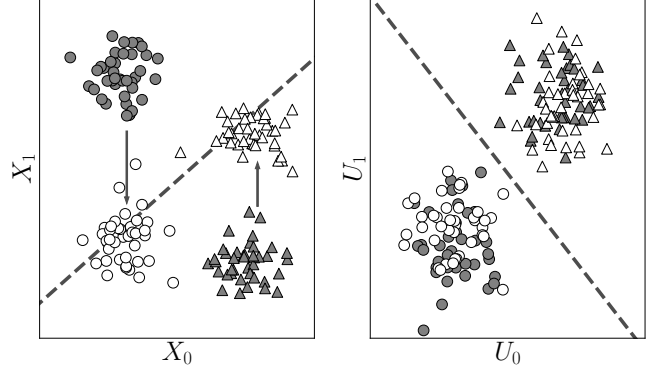


Fig. 1: Example of a domain shift and domain adaptation in an arbitrary 2-D feature space. A classification model is trained on the solid shapes, and the dashed line shows its decision boundary. The model is then applied on the hollow shapes. Due to a shift in the test domain from the training domain, the decision boundary is no longer useful. Applying a transformation $X_i \rightarrow U_i$ keeps the training and test data in similar distributions.

demonstrate an adversarial unsupervised domain adaptation technique for residential NILM settings. In [28], domain adaptation is shown as an example of a privacy-preserving measure for residential NILMs, allowing inference to be performed on a home without training on its data.

In contrast with the studies in the literature, the domains considered in this work represent different microgrid conditions, rather than different homes or facilities. Microgrids are typically designed to operate in “grid-connected” and “islanded” modes. For example, a shipboard microgrid uses its own generators while underway, and the terrestrial power grid when in port. The utility voltage waveform may vary drastically between microgrid operation modes, creating a shift in load behavior when the mode is changed. By measuring the voltage waveform, a NILM can identify grid-connected and islanded operation modes. Using either a physics-based or data-driven understanding of how grid conditions map to load behavior, this shift can be “undone” via the functional domain adaptation method presented here.

III. FEATURE SPACE COMPRESSION METHODOLOGY

Although applicable to power systems of all kinds, this work focuses on power monitoring for industrial microgrids. These grids are broadly composed of three types of loads:

- 1) Resistive elements (such as heaters)
- 2) Grid-connected induction motors
- 3) Loads with power electronic front-ends

Each of these load types has a power signature that reacts uniquely to changes in rms grid voltage. For example, resistive and linear loads obey Ohm’s law. Accordingly, their power signatures are proportional to the square of the rms voltage. By contrast, induction motors and power electronic circuits draw currents that are nonlinear in system rms voltage. In all cases, power signatures take the form of different *functions* of the rms voltage. This work presents preprocessing techniques

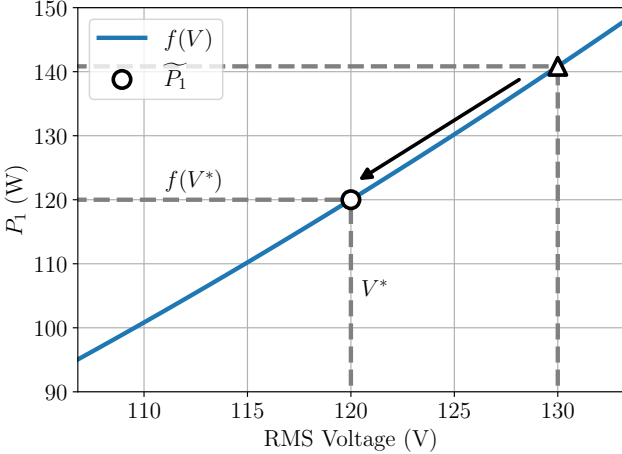


Fig. 2: Plot of real power P_1 versus rms system voltage V for a 120Ω resistive load on a nominally 120 V grid. For this load, the function $f(V) = V^2/120\Omega$ models the relationship between P_1 and V . Variance in P_1 due to changing system voltage (shown with the triangle) can be mapped to the nominal value (shown with the circle).

that account for the response of a particular load or load class to changes in system voltage. These functional preprocessors compute power signatures of arbitrary loads that are “compressed” or insensitive to system voltage changes. The result is power signatures that are more reliably classified by machine learning tools. These techniques can be further extended to other nonstationary system behavior, such as changing load torque for an electric machine, enabling physics-informed adaptation across domains and load types.

Physics-based techniques are useful since they require less data than purely data-driven techniques. Monitoring installations and retrofits on industrial grids typically do not enjoy the luxury of abundant training data, since this data would need to be collected by such a monitor.

A nonintrusive load monitor (NILM) samples the voltage and current on each phase at an aggregate point in the electrical network. All downstream electrical activity appears in the current signals sampled by the NILM. There exists a wealth of nonintrusive monitoring approaches to disaggregation and condition monitoring. This work focuses on “event-based” monitoring techniques. A NILM extracts harmonic spectral envelopes from high-bandwidth current and voltage signals [29]. Load state changes appear as geometrically unique edges in these spectral envelope streams. The NILM continuously runs an event detector to find these edges and a classifier to identify the load that produced them. Once the NILM identifies the source of each event, it extracts useful features and metrics for detecting faults and anomalous load behavior.

Steady-state power consumption is a useful feature that reveals the physical task of a load. Consider an electric motor driving a pump or ventilation system. When such a load operates less efficiently (potentially due to a clog or blockage), it may draw more real power in order to accomplish its task. However, steady-state power can also change when the system

TABLE I: Estimated parameters for the machine in Section IV.

Parameter	Value
r_s	$16.3\ \Omega$
L_{ls}	74 mH
L_{ms}	361 mH
L'_{lr}	74 mH
r'_r	$16.6\ \Omega$
ω_e	$2\pi 60\text{ rad/sec}$
V (rms line-to-line)	208 V
Rated Power	0.25 hp (184 W)
Rated slip	0.078
Rated Torque	0.6 N m
Poles	4
Rated Speed	$174\text{ rad/sec (1660 rev/min)}$

voltage level changes, potentially due to normal variations in the utility voltage waveform or changes in plant lineup. Automated fault detection algorithms can track “drift” in steady-state features as a heuristic for load condition [17]. However, these can mistakenly conclude that gradual changes in steady-state power features caused by a drifting system voltage are indicative of faulty load operation. Targeted, physics-informed preprocessing is therefore useful for automated fault detection and diagnostics.

A. Functional Signatures

Consider a load that draws in-phase and quadrature spectral envelopes P_k and Q_k at harmonic k [29]. Without loss of generality, let P_1 be modeled as some function f of the time-varying root-mean-square (rms) grid voltage V such that $P_1 = f(V)$. In practice, this rms voltage is computed over one or multiple line cycles to reject noise and fast disturbances. Let the nominal rms voltage (e.g. 120 V or 480 V) be denoted as V^* . Fig. 2 shows the graph of an example functional dependence of P_1 on V . Here, the load is a 120Ω resistor and the system’s nominal rms voltage is 120 V. To remove sensitivity to grid voltage changes, load data at voltages not equal to V^* (shown with the triangle) can be shifted to the nominal region around $(V^*, f(V^*))$ (shown with the circle). The following produces compressed spectral envelope value \tilde{P}_1 from an observed P_1 and V :

$$\tilde{P}_1 = P_1 \frac{f(V^*)}{f(V)}. \quad (1)$$

When $V = V^*$, \tilde{P}_1 is simply P_1 , since all deviations must be due to the load and not deviations in the rms voltage. When P_1 matches $f(V)$, \tilde{P}_1 is simply $f(V^*)$ since the load’s operation matches the model at that value of V .

This compression technique is linear in P_1 and as such, maintains a consistent zero point. This is beneficial for correlation score-based pattern matching. Transients representing load state changes are typically processed such that they either begin or end at zero, depending on the state change. The linearity of this technique preserves the zero point to avoid introducing biases in correlation matching.

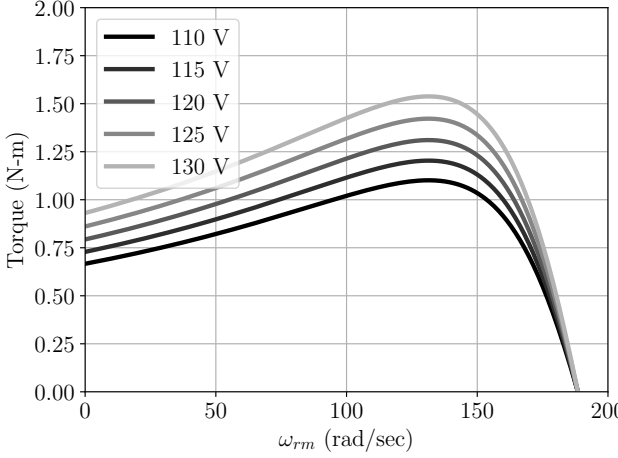


Fig. 3: Torque-speed curves with varying rms voltages for the machine in Table I.

B. Parameter-Free Compression

For a certain class of functions f , Eq. (1) reduces to a form independent of the parameters in f . Specifically, if f is a *homogeneous* function, it has the property that there is real number b associated with f such that $f(\lambda V) = \lambda^b f(V)$, where λ is any arbitrary real number [30]. For exponential functions, b is the value of the exponent. For these functions, Eq. (1) can be rewritten as follows:

$$\widetilde{P}_1 = P_1 \frac{f(V^*)}{f(V)} = P_1 \frac{f((V^*/V)V)}{f(V)}. \quad (2)$$

Then, by exploiting the homogeneity of f , this can be further reduced as follows:

$$\widetilde{P}_1 = P_1 \left(\frac{V^*}{V} \right)^b \frac{f(V)}{f(V)} = P_1 \left(\frac{V^*}{V} \right)^b. \quad (3)$$

Thus, all dependence on f vanishes. This allows for parameter-free functional compression, and forms the basis for the techniques in [5]. Examples of loads with homogeneous functions f include the following:

- Constant resistance: $f(V) \propto V^2$ ($b = 2$)
- Constant current: $f(V) \propto V$ ($b = 1$)
- Constant power: $f(V) \propto 1$ ($b = 0$)

Homogeneity is useful here because compression does not require abundant data collection or parameter estimation. Instead, compression only depends on the nominal and measured rms voltages. However, nonlinear loads such as power electronics do not have homogeneous functions. For example, constant power loads with resistive losses may take an *affine* function f of V . Depending on the makeup of the load, parameter-free compression may still provide useful but suboptimal compression. For greater compression, these loads require alternate approaches discussed in the following sections, including parameter estimation via physics-based models and data-driven characterizations.

IV. MODEL-BASED COMPRESSION

Physics-based circuit models yield constitutive equations relating voltage dropped and current drawn by a load. From

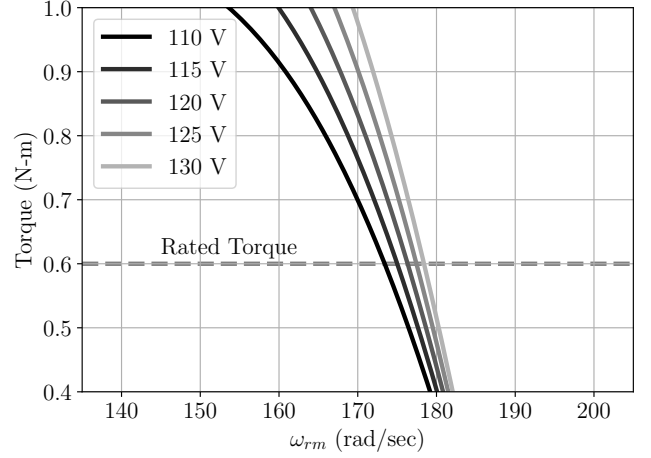


Fig. 4: Zoomed-in torque-speed curves with varying rms voltages for the machine in Table I. The dashed line shows the machine's rated load torque.

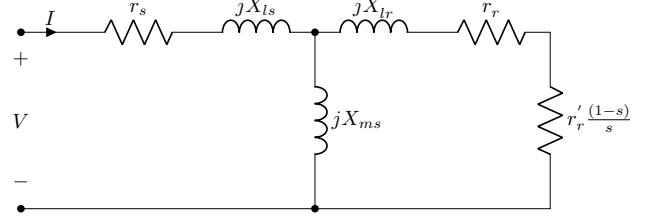


Fig. 5: Induction machine steady-state per-phase equivalent circuit with separated rotor resistances.

these equations and models, a function f relates power spectral envelope quantities to the rms grid voltage. The singly fed grid-connected induction machine serves as an example of a load with a well understood physical model whose current consumption is not necessarily linearly proportional to the rms voltage [31]. This type of machine is the workhorse electromechanical energy conversion device for industry. Around half of all consumed power flows through industrial motors [32], an application space dominated by induction machines [33]. Grid-connected induction machines are thus important targets of fault detection and diagnostic techniques enabled by power monitoring. This section uses machine analysis to characterize the nonlinear relationship between induction machine power and grid voltage. From this, a circuit model yields the function f that enables feature space compression.

A. Machine Analysis

Electrical power drawn by a grid-connected induction motor is either converted into mechanical work, stored in a magnetic field, or dissipated through resistive or magnetic core losses. The electromechanical energy conversion process is the primary contributor to the real power component of this type of machine's electrical signature. The energy conversion process converts currents and voltages (electrical power) to torque and speed (mechanical power). The rotational form

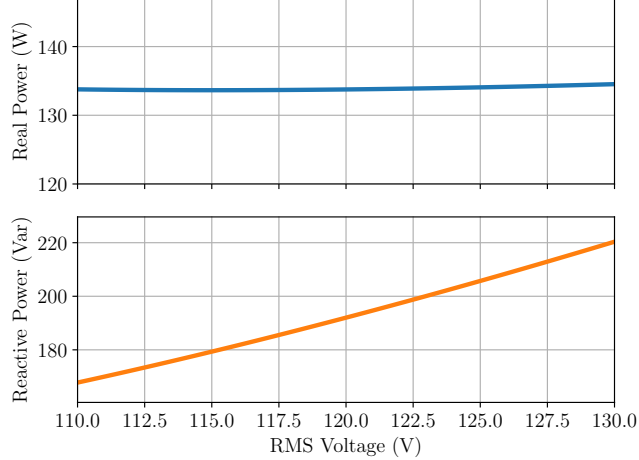


Fig. 6: Computed steady-state total real and reactive for the machine parametrized in Table I across a range of grid voltages.

of Newton's second law governs the mechanical dynamics of rotating machinery:

$$T_e = J \frac{d\omega_{rm}}{dt} + B_m \omega_{rm} + T_L, \quad (4)$$

where J is the system's rotational inertia, B_m is the mechanical damping, T_L is the load torque, T_e is the torque produced by the machine, and ω_{rm} is the shaft mechanical angular velocity. In steady state, $d\omega_{rm}/dt = 0$, reducing the equation to $T_e = B_m \omega_{rm} + T_L$. The steady-state ω_{rm} is the shaft angular velocity at which the motor develops the T_e governed by the torque-speed curve. Machine analysis often neglects damping such that $T_e \approx T_L$ [34]. If damping is not negligible, there will be additional electrical power consumption due to friction. However, for machines designed to rotate at or close to a nominal speed, this will simply add a constant offset to P_{mech} of $B_m \omega_{rm}^2$. For negligible damping, the output mechanical power is $P_{mech} = T_L \omega_{rm}$.

The following equation characterizes the torque-speed curve for this type of machine:

$$T_e = \frac{3(P/2)(X_{ms}^2/\omega_e)r'_s V^2}{[r_s r'_r + s(X_{ms}^2 - X_{ss} X'_{rr})]^2 + (r'_r X_{ss} + s r_s X'_{rr})^2}, \quad (5)$$

where P is the number of poles, $X_{ss} = X_{ls} + X_{ms}$ is the stator combined reactance, $X'_{rr} = X'_{lr} + X_{ms}$ is the rotor combined reactance (referred to the stator), ω_e is the grid frequency, and s is slip ($s = \frac{\omega_e - (P/2)\omega_{rm}}{\omega_e}$). The parameters P and X are inherent to machine construction. Across rms grid voltages, this expression yields a family of torque-speed curves [34]. Fig. 3 shows these curves for an example machine rated for 120 V (rms, line to neutral) across a 110 V to 130 V range. Table I lists the parameters of this machine.

For a machine driving a constant load torque (such as a conveyor or crane [35]), the steady-state operating point is on the right side of the torque-speed curve. Fig. 4 shows a zoomed-in version of Fig. 3 for this machine driving a 0.6 Nm load torque. The operating points occur at the intersection of

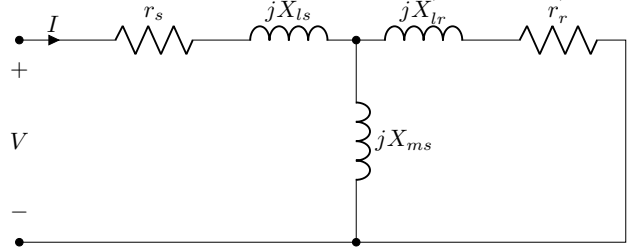


Fig. 7: Approximate induction machine per-phase inrush equivalent circuit.

the rated torque (shown with the dashed line) and each torque-speed curve. Each torque-speed curve is steep in this region, and the "spread" of ω_{rm} operating points across the range of voltage levels is small (less than 10 rad/sec). Accordingly, the spread of output power P_{mech} is also small (less than 6 W), for this constant torque load. Thus, mechanical power is nearly constant with respect to deviations in rms voltage for this type of load.

B. Steady-State Circuit Analysis

Induction machines dissipate and store energy as they deliver mechanical power. A nonintrusive monitor measures machine real and reactive power consumption which includes losses, energy storage, and electromechanical energy conversion. The steady-state induction machine circuit model predicts the salient power signatures of grid-connected machines. Fig. 5 shows the steady-state per-phase equivalent circuit of a three-phase induction machine with separated rotor resistances and ignoring core losses. Resistance r'_r models rotor conduction losses and resistance $r'_r(1-s)/s$ models electromechanical energy conversion. For constant T_L , circuit analysis or simulation yields the constitutive relation between rms voltage V and per-phase current. These yield power spectral envelopes as a function of a given rms voltage. Fig. 6 shows the steady-state real and reactive power simulated with this machine model across a range of rms voltages from 110 V to 130 V. For this machine, the real power measured by a power monitor is nearly constant, similar to the mechanical power P_{mech} .

The reactive power signature of this type of machine arises predominantly from energy storage in the magnetizing inductance. If the values of the stator and rotor resistances and reactances are negligibly small, the steady-state circuit reduces to the magnetizing inductance in parallel with the equivalent electromechanical resistance. For this case, all of the reactive power flows through the magnetizing inductance and the reactive power signature increases with the square of the grid voltage. The effects of electromechanical energy conversion and non-zero values of rotor and stator resistances add a small offset term. The model suggests that an induction machine's reactive power dependence on rms grid voltage can be described as quadratic plus a constant offset. This functional form is used later for feature space compression.

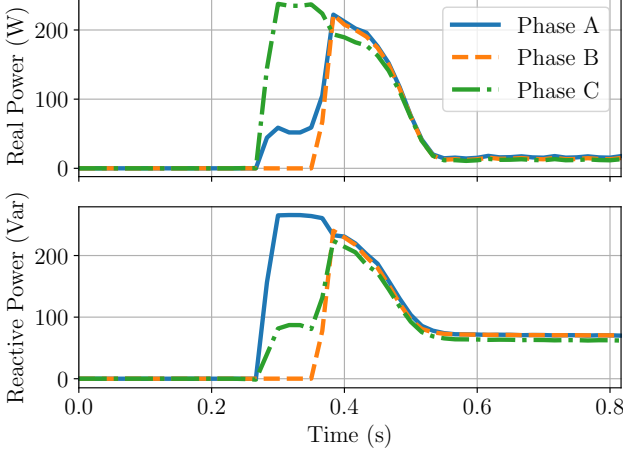


Fig. 8: Example induction motor inrush transient, shown in both real and reactive power spectral envelopes for each phase.

TABLE II: Comparison of the standard deviation (denoted as σ) of the features in Fig. 9 before and after applying model-based compression.

Feature	Original σ (W)	Compressed σ (W)	% change
P_{ss}	1.4	1.4	0
Q_{ss}	20.8	2.3	-89

C. Inrush Circuit Analysis

When an induction motor energizes, there is a sizable inrush of current required to accelerate the shaft and reach steady state. This inrush profile is a key feature for load identification and condition monitoring [36]. An example inrush transient for an induction motor is shown in Fig. 8. At $t = 0.4s$, the real and reactive powers rise sharply and decay to a steady-state value. To analyze how these features depend on rms grid voltage, assume that for a small fraction of time upon energizing, the induction machine is inertially constrained such that $\omega_{rm} = 0$. For this instant of time, the machine can be modeled with the same circuit model as the steady-state case, but with unity slip [37]. The electromechanical resistive component can therefore be replaced by a short. Fig. 7 shows the resulting circuit model. Importantly, all of the elements in this circuit model are linear and obey Ohm's law. Therefore, for the first instant of inrush current, the machine appears to the grid as a linear load with some impedance dependent on machine parameters. Unlike the steady-state power spectral envelope quantities, this feature will be proportional to the square of the rms voltage.

D. Lab Demonstration

The induction machine modeled in the previous sections was set up to drive a constant 0.6 Nm load torque. This machine was connected to a 3-phase power supply emulating a nominally 120 V (rms, line-to-neutral) grid at 60 Hz. A non-intrusive load monitor recorded phase currents and voltages at 8 kHz and then generated power spectral envelope signatures, sampled at 60 Hz. Tests were conducted at steady state across five line-to-neutral rms voltages ranging from 110 V to 130 V. Fig. 9 shows the resulting P_1 and Q_1 data in blue. Each

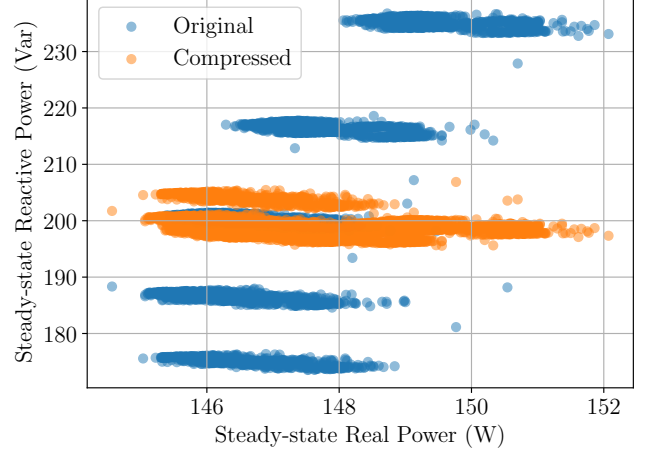


Fig. 9: Experimentally recorded steady-state real and reactive power data from the machine described in Table I. The blue points are uncompressed values. The orange points correspond to compression using the model-based polynomials in Eqs. (6) and (7). The orange points occupy a smaller region of the feature space. Due to discrepancies between model prediction and actual behavior, the bottom blue cluster (corresponding to 110 V) is compressed slightly above the rest of the compressed data around 200 Var. However, it is still much closer to the rest of the data than before compression.

discrete cluster corresponds to data at a different rms voltage level. Informed by the model shown in Fig. 6, the following functions f_P and f_Q characterize the load's steady-state real and reactive power respectively to provide compression. For real power:

$$f_P(V) = 134 \text{ W.} \quad (6)$$

As a result, the transformation in Eq. (1) is simply the identity function and this feature is not changed. For reactive power, the curve in Fig. 6 was fit with a 2nd-degree polynomial, since the circuit of Fig. 5 contains linear elements with power proportional to the square of voltage and a constant element:

$$f_Q(V) = 192 \text{ W} + (31.6 \text{ A})V + (2.98 \text{ S})V^2. \quad (7)$$

Applying Eq. (1) to both P_1 and Q_1 using f_P and f_Q respectively compresses this data into the orange cluster. This orange cluster occupies a smaller region of the feature space than the five blue clusters. Table II shows the standard deviation of both features before and after compression.

E. Shipboard Demonstration

Model parameters for loads may not always be available, especially on retrofit systems. For situations where physical parameters are unknown, the parameter-free technique of Section III-B can be applied. This technique relies on knowing the load's degree of homogeneity, which can be informed by a physics-based model. As a demonstration, the microgrid on USCGC Marlin, an 87' patrol boat, uses a single-bus configuration divided into "port" and "starboard" subpanels. These subpanels provide power to a variety of loads ancillary

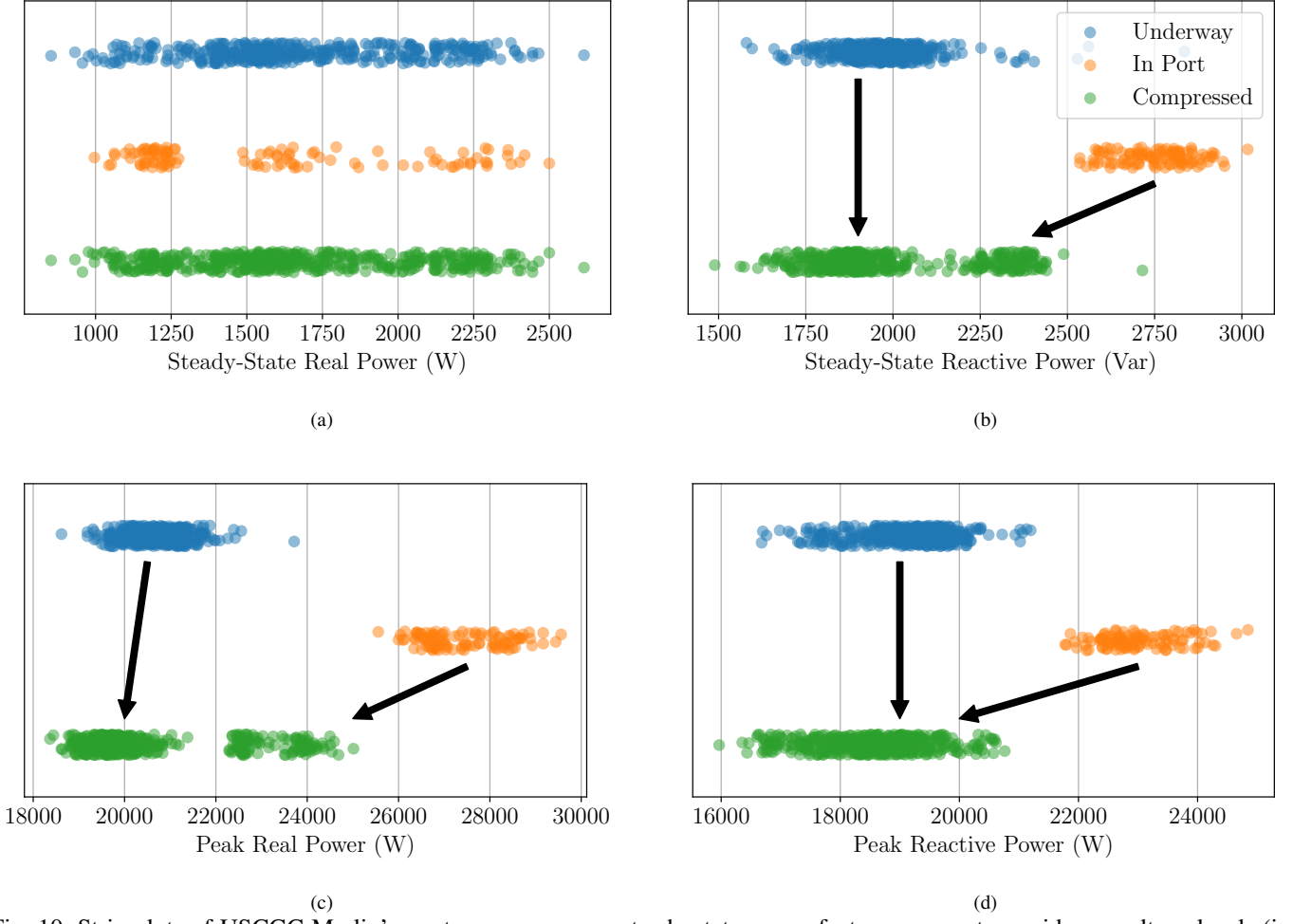


Fig. 10: Strip plots of USCGC Marlin’s waste vacuum pump steady-state power features across two grid rms voltage levels (in blue and orange) and after transforming the data with Eq (1) (in green). (a) Steady-state real power. (b) Steady-state reactive power. (c) Peak real power. (d) Peak reactive power.

to engine operation, the majority of which are heaters and induction machines [38]. A waste vacuum pump serves as a case study load for these model-based compression techniques. A three-phase, grid-connected induction machine rated at 2.5 kW drives this pump to create a vacuum in the ship’s sewage system. This pump runs automatically when the pressure in the system exceeds a setpoint. When in port, a 480 V (rms, line to line) shore tie to the terrestrial grid powers the microgrid on USCGC Marlin. When underway, onboard diesel generators power the microgrid with 450 V instead. This discrepancy in voltage levels produces two distinct power signatures for loads on this ship’s grid, including the vacuum pump. Fig. 10 shows a comparison of the distribution of steady-state and peak power features when underway (denoted “Low Voltage”) and in port (“High Voltage”), for both fundamental real and reactive power. As expected from the previous analysis, the steady-state real power distribution occupies a similar region across voltage levels, but the three other features shift drastically. Informed by the machine and circuit analysis from this section, the compression technique of Eq. (1) is applied to these four features. Since the machine parameters are unknown, the parameter-free

technique of Section III-B is applied, with $b = 0$ for the steady-state real power feature and $b = 2$ for the others. The green points in Fig. 10 show the resulting transformed distributions. In Figs. 10b, 10c, and 10d, these transformed distributions occupy smaller regions, showing a reduced variance due to voltage deviations. However, in Fig. 10a, the transformed distribution occupies the same region. As shown previously, steady-state real power is nearly independent of rms voltage deviations for this type of machine. The variance in this feature instead arises from variance in load torque, which is correctly preserved in the transformed distribution. Table III shows the standard deviations of each of these features before compression (the union of the blue and orange points) and after compression (the green points).

V. DATA-DRIVEN COMPRESSION

Although loads such as heaters and grid-connected machines can be reasonably modeled with lumped parameter circuit equivalents, more complicated loads make this approach intractable or impractical. For these loads, empirical characterizations of $f(V)$ provide tailored compression using

TABLE III: Comparison of the standard deviation (denoted as σ) of the features in Fig. 10 before and after applying parameter-free compression.

Feature	Original σ (W)	Compressed σ (W)	% change
P_{ss}	376.4	376.4	0
Q_{ss}	345.4	214.8	-37.8
P_{pk}	2843.5	1548.6	-45.5
Q_{pk}	1772.8	863.2	-51.3

data collected either *in situ* or in simulation. This section demonstrates this technique with a constant power dc load.

A. Rectifier Analysis

Power electronic loads, such as variable speed motor drives, battery chargers, and computers, typically use a diode bridge rectifier to interface with the ac grid. Fig. 11 shows the circuit schematic of a generic three-phase grid-connected rectifier. This rectifier powers an arbitrary dc load consuming power P_{dc} . Simulating this circuit with a P_{dc} of 220 W across a range of rms voltages shows that this load has a nearly constant steady-state real power consumption. This matches intuition, since the constant value of P_{dc} makes it effectively a constant power load.

However, a telltale feature set for power electronics is the current drawn at harmonic multiples of the grid frequency. These current harmonics arise from the nonlinear nature of switching components. As the rms voltage changes, the firing times of the diodes on this passive rectifier will also change. Thus, the relationship between current harmonics and rms system voltage is potentially more complicated than simply being constant. To illustrate, Fig. 12 shows the values of the in-phase fifth and seventh harmonic currents (scaled by the rms voltage to form P_5 and P_7) across five rms voltages from 110 V to 130 V. Most power electronic loads draw currents that are half-wave symmetric, meaning that only odd harmonics have any spectral content. Fifth and seventh harmonics are examined here because third harmonics are ideally zero on a balanced three-phase system. These two harmonics have two distinct dependencies on V that are both non-constant. A NILM monitored the currents into a Matsusada RE series 45 V 45 A three-phase ac-to-dc power supply [39]. This power supply uses a three-phase diode bridge rectifier with an input filter, and resembles the circuit in Fig. 11. For a constant P_{dc} of 220 W (drawn using an electronic load), Fig. 13 shows values of P_5 and P_7 versus rms voltage collected experimentally. The trends of this data matches the simulated data in Fig. 12, showing that the fifth and seventh harmonics have different dependencies on V . Therefore, an opportunity exists to compress these harmonics using a function $f(V)$ that describes them.

Deriving a closed-form $f(V)$ for these harmonics is algebraically tedious. Instead, data-driven function approximators such as linear regression, polynomial fit, and artificial neural networks can provide an estimate using data collected either empirically or in simulation. For demonstration purposes, consider 2nd-degree polynomials fit via least squares to the fifth and seventh harmonics, for both the simulated data in Fig. 12 and experimental data of Fig. 13. Applying Eq. (1) to

Algorithm 1 Load matching algorithm before introducing domain adaptation.

Input: Observed power transient P
Output: Best matching load l^*

- 1: bestMatchScore $\leftarrow 0$
- 2: **for each** load **do**
- 3: matchScore \leftarrow correlationMatch(P , load.exemplar)
- 4: **if** matchScore $>$ bestMatchScore **then**
- 5: $l^* \leftarrow$ load
- 6: bestMatchScore \leftarrow matchScore
- 7: **end if**
- 8: **end for**

the fifth and seventh harmonic data using these functions yields the plot in Fig. 14. The blue data points represent the original, uncompressed in-phase seventh versus fifth harmonic data. The orange points represent these same points after compression with the function fit on simulation data. The green points show these points after compression with the function fit on experimental data. Due to the simulation model not perfectly matching the actual hardware, the experimental data-informed function provides the most compression.

VI. IMPLEMENTATION

Load identification in industrial NILMs typically involves geometric correlation matching between observed transient data and “exemplar” transients representative of each possible load state change [19]. These transients traditionally use a common set of features (such as fundamental real and reactive spectral envelopes). To accommodate the feature space compression techniques presented here, this framework needs modification. Algorithm 1 shows pseudocode for the existing classification scheme used by NILMs deployed in industrial settings. Each load state change has its own exemplar, and a NILM matches every transient event it records to an exemplar. To do so, the NILM performs a correlation match between the transient and every exemplar. The NILM then selects the exemplar with the highest correlation score as the best match. To accommodate the preprocessing techniques developed in this work, Algorithm 2 shows a modified version of this scheme. Before the correlation matching function is called for each load, that load’s compression technique preprocesses the transient signature and load exemplar. This can be done point-by-point for every timestep in both the exemplar and observed transient signature. The rest of the procedure remains the same.

A. Choosing a Compression Technique

Choosing a compression technique requires knowledge of a load’s behavior, either from a physics-based model or from empirical data. If the characteristics of a load are completely unknown to an operator, a compression technique cannot be chosen *a priori*. This section provides a guide for selecting an appropriate compression function for a given load monitoring application.

Parameter-free compression is ideal for loads whose power spectral envelopes are homogeneous functions of grid voltage.

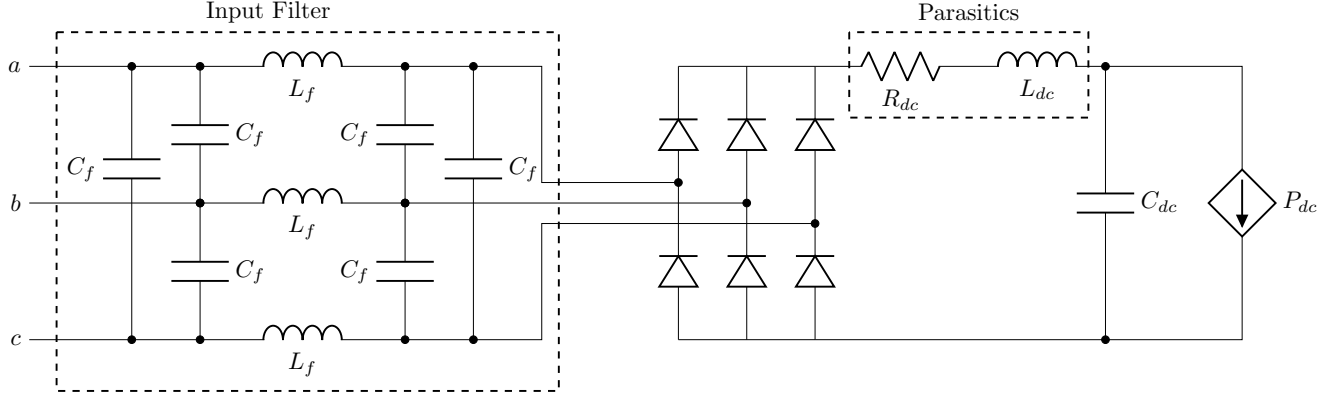


Fig. 11: Circuit schematic for a passive dc rectifier with parasitic components and an input filter.

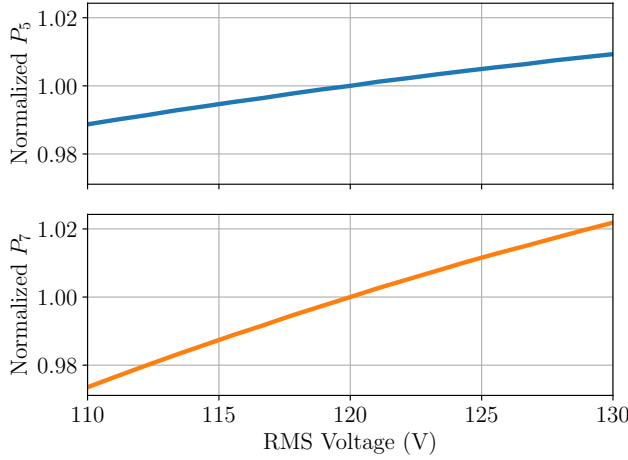


Fig. 12: Normalized in-phase fifth and seventh harmonic power spectral envelopes versus rms system voltage collected in simulation of Fig. 11.

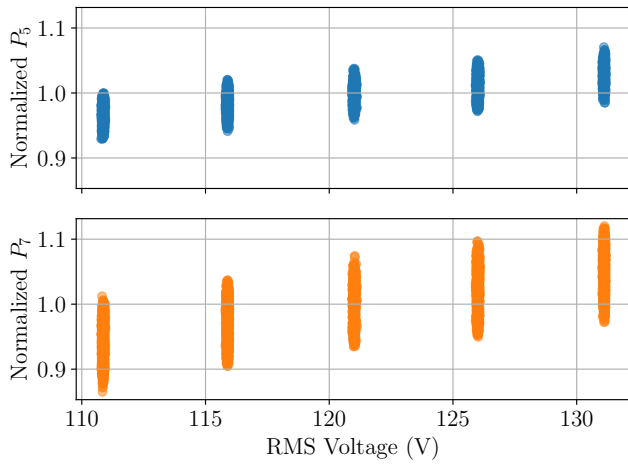


Fig. 13: Normalized in-phase fifth and seventh harmonic power spectral envelopes versus rms system voltage, collected experimentally with a NILM.

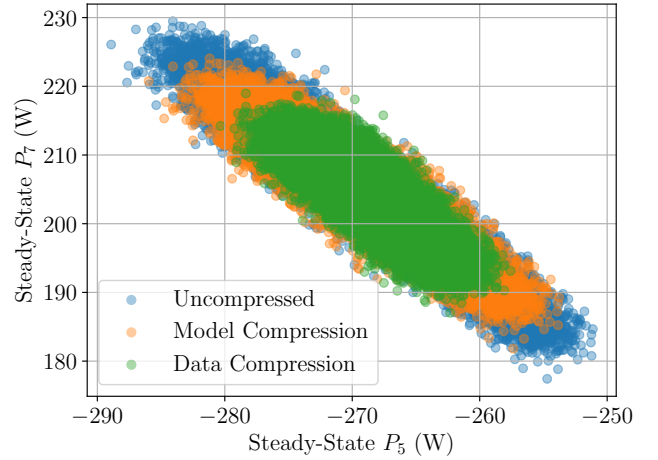


Fig. 14: Steady-state total P_7 versus P_5 for the dc power supply. The blue points show the raw steady-state harmonic values, and the orange and green points show the compressed values.

Algorithm 2 Load matching algorithm after introducing domain adaptation.

Input: Observed power transient P
Output: Best matching load l^*

- 1: bestMatchScore $\leftarrow 0$
- 2: **for** each load **do**
- 3: $\tilde{P} \leftarrow \text{load.compress}(P)$ ▷ Using Eq. (1)
- 4: exemplar $\leftarrow \text{load.compress}(\text{load.exemplar})$
- 5: matchScore $\leftarrow \text{correlationMatch}(\tilde{P}, \text{exemplar})$
- 6: **if** matchScore > bestMatchScore **then**
- 7: $l^* \leftarrow \text{load}$
- 8: bestMatchScore $\leftarrow \text{matchScore}$
- 9: **end if**
- 10: **end for**

Loads known to be linear, such as resistors, capacitors, and inductors are the simplest case. Linear loads' power spectral envelopes are proportional to the square of the grid voltage. In addition, constant current loads have a magnitude and phase

independent of voltage, making their power spectral envelopes proportional to the grid voltage. Constant power loads consume a constant real and reactive power independent of grid voltage. In each of these cases, parameter-free compression completely removes the variance due to changing grid voltage.

Many loads, however, such as electromechanical and switching power electronic loads, have more complicated dependencies on system voltage. These dependencies can be characterized either with parameterized physics-based models or power data collected across several grid voltages. However, if parameters and data are unavailable, heuristic information on a load may allow partial parameter-free compression. For example, a load known to have a combination of constant power and resistive components may still be suboptimally compressed with the parameter-free method, due to the variation in the resistive component.

As a concrete example, consider the induction machine in Section IV. If all that is known is that the machine is a grid-connected induction machine, parameter-free compression can be applied to peak and steady-state features, as was done for the shipboard pump in Section IV-E. Although only some of the variance is reduced, this provides a useful starting point before data is collected and parameters are identified. If machine parameters become known, the process described in Section IV-D can be applied to obtain better compression using the equations for peak and steady-state real and reactive powers. If parameters are never known but the operator can identify a large set of load events in a dataset, the technique of Section V can be applied to fit an empirical model to the data (rather than using a parameterized equation such as Eq. (5)).

B. Computational Costs

Applying the compression technique increases the inference time for each classified event. Eq. (1) is applied to the incoming transient signature at the observed voltage V . For the model-based and data-driven techniques, this requires evaluating $f(V)$ and $f(V^*)$, which can be precomputed ahead of time for the nominal voltage V^* . One multiplication and one division operation are then required to preprocess every point in the transient. Parameter-free compression using Eq. (3) requires a division, a multiplication, and an exponentiation. Real-time use of this technique requires that this can be performed fast enough that compressing one transient does not block compressing the next transient event. However, on modern computing hardware, applying these three steps (function evaluation or exponentiation, multiplication, and division) are practically instant when compared to the time a NILM will spend between transient events – often on the order of seconds or minutes.

VII. CONCLUSION

Data variability unrelated to load condition frustrates non-intrusive condition monitoring, especially on microgrids with changing conditions. The techniques presented in this work provide physics- and data-informed preprocessing techniques to mitigate these effects, using system voltage as a case study. The case studies presented in this work achieve reductions

in feature standard deviations from 37.8% to 89% on grids with changing voltages. Future work involves applying the techniques presented here to reduce data variance caused by other changes in grid conditions. These may include evolving temperatures, load torques, and system frequencies. For example, induction motors that operate with two different torque profiles may be compressed into one consistent signature using physically informed analysis.

ACKNOWLEDGMENTS

We gratefully acknowledge the support and dedication of the US Coast Guard and in particular the crew of USCGC Marlin. We also gratefully acknowledge the support of the Office of Naval Research NEPTUNE program.

REFERENCES

- [1] K. Ashok, D. Li, N. Gebraeel, and D. Divan, “Online detection of interturn winding faults in single-phase distribution transformers using smart meter data,” *IEEE Transactions on Smart Grid*, vol. 12, no. 6, pp. 5073–5083, 2021.
- [2] A. Gao, F. Mei, J. Zheng, H. Sha, M. Guo, and Y. Xie, “Electricity theft detection based on contrastive learning and non-intrusive load monitoring,” *IEEE Transactions on Smart Grid*, vol. 14, no. 6, pp. 4565–4580, 2023.
- [3] J. Paris, J. S. Donnal, R. Cox, and S. Leeb, “Hunting cyclic energy wasters,” *IEEE Transactions on Smart Grid*, vol. 5, no. 6, pp. 2777–2786, 2014.
- [4] S. Tang, S. Yuan, and Y. Zhu, “Data preprocessing techniques in convolutional neural network based on fault diagnosis towards rotating machinery,” *IEEE Access*, vol. 8, pp. 149487–149496, 2020.
- [5] A. W. Langham, T. C. Krause, D. H. Green, and S. B. Leeb, “Multistream power monitoring for energy systems,” *IEEE Transactions on Smart Grid*, pp. 1–1, 2024.
- [6] *IEEE Standard for Interconnection and Interoperability of Distributed Energy Resources with Associated Electric Power Systems Interfaces*, IEEE Std., 2018.
- [7] G. Hart, “Nonintrusive appliance load monitoring,” *Proceedings of the IEEE*, vol. 80, no. 12, pp. 1870–1891, 1992.
- [8] J. Kelly and W. Knottenbelt, “The UK-DALE dataset, domestic appliance-level electricity demand and whole-house demand from five uk homes,” *Scientific Data*, vol. 2, no. 1, p. 150007, Mar. 2015.
- [9] J. De La Ree, V. Centeno, J. S. Thorp, and A. G. Phadke, “Synchronized phasor measurement applications in power systems,” *IEEE Transactions on Smart Grid*, vol. 1, no. 1, pp. 20–27, 2010.
- [10] R. Rashed Mohassel, A. Fung, F. Mohammadi, and K. Raahemifar, “A survey on advanced metering infrastructure,” *International Journal of Electrical Power & Energy Systems*, vol. 63, pp. 473–484, 2014.
- [11] H. Mohsenian-Rad and W. Xu, “Synchro-waveforms: A window to the future of power systems data analytics,” *IEEE Power and Energy Magazine*, vol. 21, no. 5, pp. 68–77, 2023.
- [12] A. Ridi, C. Gisler, and J. Hennebert, “A survey on intrusive load monitoring for appliance recognition,” in *2014 22nd International Conference on Pattern Recognition*, 2014, pp. 3702–3707.
- [13] P. A. Schirmer and I. Mporas, “Non-intrusive load monitoring: A review,” *IEEE Transactions on Smart Grid*, vol. 14, no. 1, pp. 769–784, 2023.
- [14] “Sense - Control your home energy use,” <https://sense.com/>, accessed: 2025-04-01.
- [15] J. Kelly and W. Knottenbelt, “Neural NILM: Deep neural networks applied to energy disaggregation,” in *Proceedings of the 2nd ACM International Conference on Embedded Systems for Energy-Efficient Built Environments*, ser. BuildSys ’15. New York, NY, USA: Association for Computing Machinery, 2015, p. 55–64.
- [16] J. Z. Kolter and M. J. Johnson, “REDD: A public data set for energy disaggregation research,” in *Proceedings of the SustKDD workshop on Data Mining Applications in Sustainability*, 2011.
- [17] D. H. Green, A. W. Langham, R. A. Agustin, D. W. Quinn, and S. B. Leeb, “Adaptation for automated drift detection in electromechanical machine monitoring,” *IEEE Transactions on Neural Networks and Learning Systems*, vol. 34, no. 10, pp. 6768–6782, 2023.

- [18] ——, “Physics-informed feature space evaluation for diagnostic power monitoring,” *IEEE Transactions on Industrial Informatics*, vol. 19, no. 3, pp. 2363–2373, 2023.
- [19] D. H. Green, S. R. Shaw, P. Lindahl, T. J. Kane, J. S. Donnal, and S. B. Leeb, “A multiscale framework for nonintrusive load identification,” *IEEE Transactions on Industrial Informatics*, vol. 16, no. 2, pp. 992–1002, 2020.
- [20] S. Zhang, S. Zhang, B. Wang, and T. G. Habetler, “Deep learning algorithms for bearing fault diagnostics—a comprehensive review,” *IEEE Access*, vol. 8, pp. 29 857–29 881, 2020.
- [21] D. H. Green, P. A. Lindahl, and S. B. Leeb, “Three-phase electrical measurement representations for nonintrusive load diagnostics,” *IEEE Open Journal of Instrumentation and Measurement*, vol. 1, pp. 1–14, 2022.
- [22] S. Chen, L. Han, X. Liu, Z. He, and X. Yang, “Subspace distribution adaptation frameworks for domain adaptation,” *IEEE Transactions on Neural Networks and Learning Systems*, vol. 31, no. 12, pp. 5204–5218, 2020.
- [23] R. Tan and W. Luo, “Physics-informed machine learning model generalization in AIoT: Opportunites and challenges,” in *Proceedings of Cyber-Physical Systems and Internet of Things Week 2023*, ser. CPS-IoT Week ’23. New York, NY, USA: Association for Computing Machinery, 2023, p. 170–176.
- [24] A. Farahani, S. Voghoei, K. Rasheed, and H. R. Arabnia, “A brief review of domain adaptation,” in *Advances in Data Science and Information Engineering*, R. Stahlbock, G. M. Weiss, M. Abou-Nasr, C.-Y. Yang, H. R. Arabnia, and L. Deligiannidis, Eds. Cham: Springer International Publishing, 2021, pp. 877–894.
- [25] M. Muaz, I. Zinnikus, and M. Shahid, “NILM domain adaptation: When does it work?” in *2024 10th International Conference on Smart Computing and Communication (ICSCC)*, 2024, pp. 524–528.
- [26] J. Lin, J. Ma, J. Zhu, and H. Liang, “Deep domain adaptation for non-intrusive load monitoring based on a knowledge transfer learning network,” *IEEE Transactions on Smart Grid*, vol. 13, no. 1, pp. 280–292, 2022.
- [27] Y. Liu, L. Zhong, J. Qiu, J. Lu, and W. Wang, “Unsupervised domain adaptation for nonintrusive load monitoring via adversarial and joint adaptation network,” *IEEE Transactions on Industrial Informatics*, vol. 18, no. 1, pp. 266–277, 2022.
- [28] P. Hao, Z. Yan, and H. Wen, “Privacy-preserving NILM: A self-alignment source-aware domain adaptation approach,” *IEEE Transactions on Instrumentation and Measurement*, vol. 74, pp. 1–12, 2025.
- [29] J. Paris, J. S. Donnal, Z. Remscrim, S. B. Leeb, and S. R. Shaw, “The sinefit spectral envelope preprocessor,” *IEEE Sensors Journal*, vol. 14, no. 12, pp. 4385–4394, 2014.
- [30] A. Polyakov, “Introduction,” in *Generalized Homogeneity in Systems and Control*. Cham: Springer International Publishing, 2020, pp. 1–21.
- [31] H. L. Willis, *Power distribution planning reference book*, 2nd ed., ser. Power engineering : 1. New York: Marcel Dekker, 2004.
- [32] P. Waide and C. U. Brunner, “Energy-efficiency policy opportunities for electric motor-driven systems,” 2011.
- [33] F. Immovilli, C. Bianchini, M. Cocconcelli, A. Bellini, and R. Rubini, “Bearing fault model for induction motor with externally induced vibration,” *IEEE Transactions on Industrial Electronics*, vol. 60, no. 8, pp. 3408–3418, 2013.
- [34] P. C. Krause and T. C. Krause, *Introduction to Modern Analysis of Electric Machines and Drives*. Hoboken, New Jersey: Wiley-IEEE Press, 2023.
- [35] C. M. Vega Gonzalez, J. Rodriguez Arribas, and D. Ramirez Prieto, “Optimal regulation of electric drives with constant load torque,” *IEEE Transactions on Industrial Electronics*, vol. 53, no. 6, pp. 1762–1769, 2006.
- [36] E. K. Saathoff, D. H. Green, R. A. Agustin, J. W. O’Connell, and S. B. Leeb, “Inrush current measurement for transient space characterization and fault detection,” *IEEE Transactions on Instrumentation and Measurement*, vol. 70, pp. 1–10, 2021.
- [37] S. R. Shaw, “Numerical methods for identification of induction motor parameters,” Master’s thesis, Massachusetts Institute of Technology, February 1997.
- [38] B. Mills, “Solving Time-Alignment Challenges in Shipboard Non-Intrusive Load Monitoring,” Master’s thesis, Massachusetts Institute of Technology, 2021.
- [39] Matsusada Precision Inc., “Dc power supplies — re series.” [Online]. Available: <https://www.matsusada.com/product/dc-power-supplies/rack/re/>



Aaron W. Langham (Graduate Student Member, IEEE) received the B.E.E. degree in electrical engineering from Auburn University, Auburn, AL, USA in 2018, and the M.S. and E.E. degrees in electrical engineering and computer science from the Massachusetts Institute of Technology, Cambridge, MA, USA in 2022 and 2024, respectively. He is currently pursuing the Ph.D. degree in electrical engineering and computer science at the Massachusetts Institute of Technology, Cambridge, MA, USA. His research interests include signal processing, machine learning, and IoT platforms for energy systems.



Thomas C. Krause (Graduate Student Member, IEEE) received the B.S. degree in electrical engineering from Purdue University, West Lafayette, IN, USA, in 2019, and the M.S. and E.E. degrees in electrical engineering and computer science from the Massachusetts Institute of Technology, Cambridge, MA, USA, in 2021 and 2024, respectively, where he is currently pursuing the Ph.D. degree.



Steven B. Leeb received the Ph.D. degree from the Massachusetts Institute of Technology, in 1993. Since 1993, he has been a member on the MIT Faculty with the Department of Electrical Engineering and Computer Science. He also holds a joint appointment with the Department of Mechanical Engineering, MIT. He is concerned with the development of signal processing algorithms for energy and real-time control applications.